Progress In Electromagnetics Research C, Vol. 133, 233–249, 2023

A Control Method of Switched Reluctance Motor Based on Non-Unity TSF and Adaptive Overlapping Angle

Chaozhi Huang, Wensheng Cao*, Yanwen Sun, Zhou Chen, and Wenjin Zhang

Abstract—Aiming at the problems of conventional torque sharing function (TSF) control method, such as large torque ripple, high peak current, and high copper loss, a non-unity TSF control method with adaptive overlapping angle is proposed. Firstly, on the basis of explaining the conventional TSF control logic, according to the characteristics of inductance, the conduction region is redivided, and the two-phase exchange region is subdivided into region 1 and region 2, which together with the single-phase conduction region form three regions in the winding conduction region. A non-unity TSF is designed in each region, which conforms to the torque variation trend. Then, an adaptive overlapping angle algorithm is designed, which can automatically adjust the overlapping angle under different speeds and load torques. Finally, taking a three-phase 6/20-pole switched reluctance motor as the control object, the simulation and experimental verification show that the control method can restrain torque ripple and reduce peak current and copper loss at the same time.

1. INTRODUCTION

In recent years, switched reluctance motor (SRM) has been widely used in various electric drive fields, especially in the field of electric vehicles, because of its advantages of simple structure, low cost, reliable performance, and wide speed range [1–3]. Reference [4] applies SRM to electric vehicles, and the motor operates smoothly at a wider speed range. In [5], aiming at the application of a four-phase SRM in electric vehicles, a new integrated power converter is proposed, which can drive the operation of SRM efficiently while reducing current sensors. However, the double salient pole structure and switching conduction mode of SRM make the motor have large torque ripple and peak current, which hinders its further popularization and application.

Torque ripple control methods of SRM include direct torque control (DTC), angular position control (APC), current chopping control (CCC), pulse width modulation (PWM) control, torque sharing function control (TSF), etc. In [6], DTC method is applied to SRM for the first time, which reduces the torque ripple of motor. In [7], an improved DTC method is proposed, which reduces torque ripple by modifying sector division and voltage vector. In [8], the voltage vector table is improved accordingly, and the optimized DTC can effectively reduce torque ripple. In [9, 10], APC method is used, but APC control method only controls the opening angle, which will produce large torque ripple. CCC control method has the advantages of simple control and strong reliability, but larger torque ripple limits its further application [11, 12]. In [13–15], a fixed-frequency PWM controller is applied to the control of SRM, and on this basis, the proportional-integral (PI) current controller or iterative learning is optimized to reduce the generation of torque ripple.

Among numerous control methods, TSF method is a common and effective method. In [16], four kinds of conventional TSF are compared and analyzed, and further optimized to reduce torque ripple.

Received 18 February 2023, Accepted 15 May 2023, Scheduled 16 June 2023

* Corresponding author: Wensheng Cao (cwscaowensheng@163.com).
The authors are with the College of Electrical and Automation, Jiangxi University of Science and Technology, Ganzhou 341000, China.

In [17], based on the neural network model, through angle parameters and off-line design, the improved TSF is obtained. In [18], the torque ripple is reduced by off-line optimization of TSF, so as to obtain the best TSF. In [19], the vector table is optimized by combining TSF and model prediction, which reduces the generation of torque ripple, but the peak current is large. Ref. [20] proposes online compensation TSF to compensate demagnetization phase and excitation phase accordingly, which reduces the generation of torque ripple but does not consider the influence of peak current and copper loss. In [21], an improved TSF control method is proposed. The new TSF function is more in line with the trend of torque change, but it does not consider the influence of copper loss, resulting in a larger peak current. In [22], fuzzy control TSF is put forward by combining fuzzy control with TSF. Although torque ripple can be effectively suppressed, copper loss increases accordingly, reducing the efficiency of the motor. In the above control methods, it is difficult to optimize these problems at the same time: reduction of torque ripple, peak current, and copper loss.

In order to reduce the torque ripple, peak current, and copper loss of SRM, this paper proposes a non-unity TSF method with adaptive overlapping angle (non-unity TSF-AOA). Firstly, the characteristics of inductance and torque variation of SRM are analyzed. Secondly, according to the difference of inductance change rate, the conduction region is divided into three regions, and the corresponding non-unity TSF is proposed in each new region to suppress the torque ripple. Then, by using the proposed adaptive algorithm of overlapping angle, the overlapping angle can be automatically adjusted under different speeds and load torques, thus reducing copper loss. Finally, through simulation and experimental verification, the current waveform and torque waveform under different speeds and load torques are compared, which verifies the effectiveness of the control method in reducing torque ripple, peak current, and copper loss.

2. MATHEMATICAL MODEL OF SRM

According to the electromechanical conversion principle, the main formulas of SRM include voltage balance equation, mechanical equation, and electromechanical connection equation.

The k-th phase voltage balance equation of SRM is as follows:

$$U_k = R_k i_k + \frac{d\varphi_k}{dt} \tag{1}$$

In the above formula, U_k, R_k, i_k, and φ_k are the voltage, resistance, current, and flux linkage of the k-th phase winding, respectively.

The motion formula can be expressed as follows:

$$T_e = J\frac{d^2\theta}{dt} + D\frac{d\theta}{dt} + T_L \tag{2}$$

where T_e, J, D, and T_L are electromagnetic torque, rotary inertia, rubbing factor, and load torque.

Electromechanical connection equation of SRM is as follows:

$$T_x = \frac{\partial W'\left(\theta, i\right)}{\partial\theta}|_{i=\text{const}} \tag{3}$$

In the formula, W' is the total magnetic energy, and θ is the rotor position angle. The expression of electromagnetic torque of SRM can be obtained by changing formula (3), which is convenient for qualitative analysis of torque change characteristics. The specific formula is:

$$T_x = \frac{1}{2}i(k)^2\frac{\partial L(k)}{\partial\theta} \tag{4}$$

3. CONVENTIONAL TSF CONTROL

3.1. Conventional TSF Control System

TSF control method is a common method which reduces torque ripple of SRM. The specific control system structure is shown in Figure 1. Firstly, the torque reference T_{ref} which is generated by the speed loop defines the torque reference T_k^* of each phase through the torque sharing function. Then the

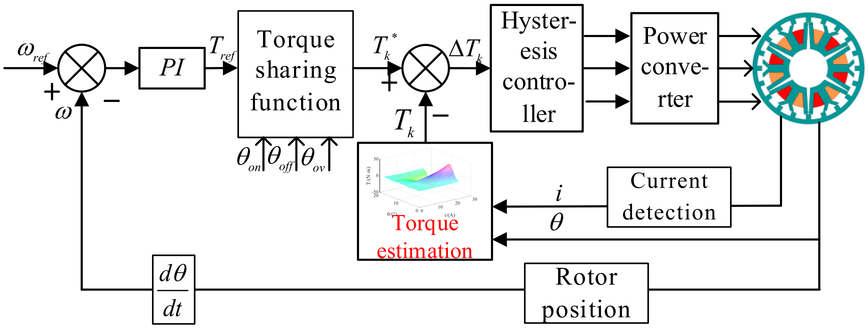

Figure 1. Block diagram of the conventional TSF system.

actual torque value T_k is calculated through the detection of current and rotor position. Finally, the obtained torque error ΔT is input into the hysteresis controller to control the switching state of each phase, which is beneficial for the actual torque following the torque reference, maintaining the stability of the total torque and reducing torque ripple.

The TSF module in Figure 1 takes the total torque reference T_{ref}, rotor position angle θ, turn-on angle (θ_{on}), turn-off angle (θ_{off}), and the overlapping angle (θ_{ov}) as inputs, and obtains the torque reference of each phase through TSF. The distribution function of phase $k(f_k(\theta))$ needs to satisfy the following three conditions:

$$\begin{cases} T_k(\theta) = T_{ref} f_k(\theta) \\ \displaystyle\sum_{k=1}^{3} f_k(\theta) = 1 \\ 0 \leq f_k(\theta) \leq 1 \end{cases} \tag{5}$$

The common TSF types are linear, cubic, exponential, and cosine. The exponential torque ripple suppression effect is the best, and the expression is as follows:

$$f_k(\theta) = \begin{cases} 0 & 0 \leq \theta < \theta_{on} \\ q_{up}(\theta) = 1 - e^{\left(\frac{-(\theta-\theta_{on})^2}{\theta_{ov}}\right)} & \theta_{on} \leq \theta < \theta_{on} + \theta_{ov} \\ 1 & \theta_{on} + \theta_{ov} \leq \theta < \theta_{off} \\ q_{down}(\theta) = e^{\left(\frac{-(\theta-\theta_{off})^2}{\theta_{ov}}\right)} & \theta_{off} \leq \theta < \theta_{off} + \theta_{ov} \\ 0 & \theta_{off} + \theta_{ov} \leq \theta < \tau_r \end{cases} \tag{6}$$

where τ_r is the rotor pole pitch, and $q_{up}(\theta)$ and $q_{down}(\theta)$ are the rising section function and falling section function of TSF, respectively.

In SRM, the region where single-phase conduction current provides torque is called single-phase conduction (SpC) region, and the region where two-phase conduction current provides torque is called two-phase exchange (TpE) region. In the TpE, the phase with rising current is called excitation phase, and the phase with falling current is called demagnetization phase. In the SpC and TpE, the switching state of each phase power converter is determined according to the torque error hysteresis.

3.2. Inductance and Torque Characteristics

According to formula (4), the generation of SRM torque is influenced by the partial derivative of inductance (L) to angle (θ). Through finite element simulation, the inductance curve and its partial derivative are obtained. Take $I = 10\,\mathrm{A}$ as an example, as shown in Figure 2.

As can be seen from Figure 2, there are low inductance region and high inductance region in the conduction region of SRM, and the value of inductance change rate $\partial L/\partial\theta$ in the low inductance region is small, while the value of $\partial L/\partial\theta$ is large in the high inductance region. According to formula (4), the

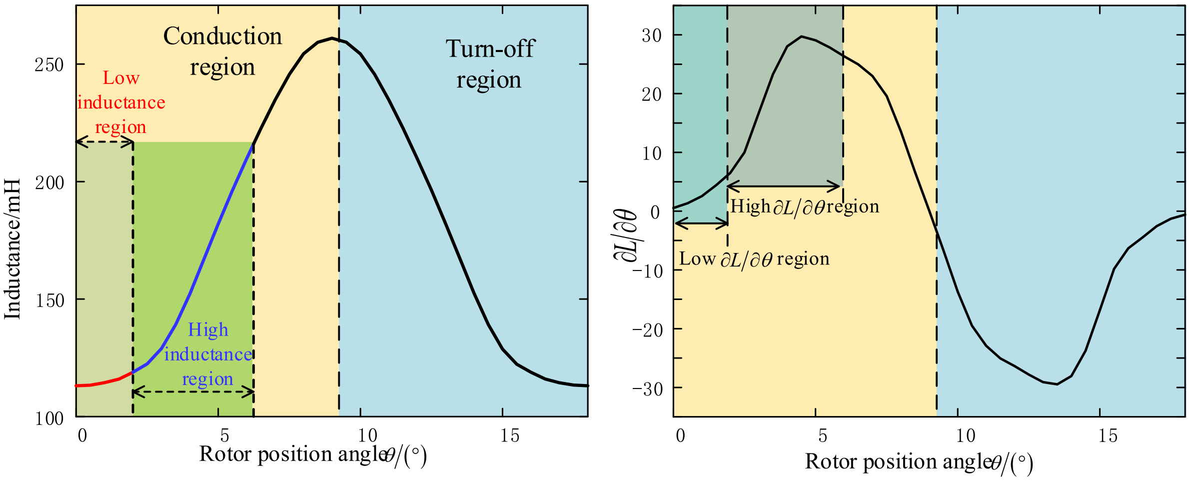

Figure 2. Inductance curve and $\partial L/\partial\theta$ curve.

conduction of the excitation phase winding in the low inductance region will lead to insufficient torque of the excitation phase, and at this time, the demagnetization phase will also enter the demagnetization state, and the generated torque will gradually decrease, resulting in insufficient torque and torque ripple. In the region with high inductance, the current of the excitation phase becomes larger, and the excitation phase has enough capacity to generate torque. If the demagnetization phase torque cannot be reduced in time, it is easy to cause the synthetic torque to be large, leading to torque ripple.

The conventional TSF will distribute a large torque to the excitation in the small inductance region, but it is difficult for the excitation phase to provide the required torque in this region. In the region of large inductance, the function assigned by conventional TSF to the demagnetization phase cannot make the demagnetization phase drop quickly, and there is still a large torque, which is difficult to meet the requirements of torque reduction. Both of the above conditions lead to large torque ripple. In addition, the arbitrariness of the overlapping angle will also lead to peak current, further increasing the copper loss of the motor and reducing the efficiency of the motor. Therefore, a non-unity TSF control method with adaptive overlapping angle is proposed.

4. PROPOSED NON-UNITY TSF

4.1. Non-Unity TSF

From the previous analysis, it can be seen that the inductance characteristics of the low inductance region and high inductance region are different in the conduction area, which makes it difficult for the conventional TSF control method to keep the torque stable. So, it is necessary to design TSF in different regions according to the characteristics of inductance curve. The new region allocation is shown in Figure 3.

In Figure 3, the TpE is refined two regions, and together with the SpC forms three regions in the winding conduction area. Taking phase B as an example, the inductance changes obviously at θ_u^B (the inductance mutation point). So the TpE is divided into two regions with θ_u^B as the boundary. The area before θ_u^B is called region 1. The starting point of region 1 is the turn-on angle θ_{on}^B, and the end point is θ_u^B. The region after θ_u^B is called region 2. The starting point of region 2 is θ_u^B, and the ending point is the sum of the turn-on angle and the overlapping angle $\theta_{on}^B + \theta_{ov}$ which is calculated by the adaptive overlapping angle algorithm. At the end of region 2 $\theta_{on}^B + \theta_{ov}$, the demagnetization phase current drops to 0, then entering the SpC of the excitation phase. The regions distributions of other phases are similar.

Based on the new region allocation, the TSF of demagnetizing phase and exciting phase suitable for this region are designed to reduce the torque ripple. Taking phase A as demagnetizing phase and phase B as exciting phase, the specific TSF in each section is as follows:

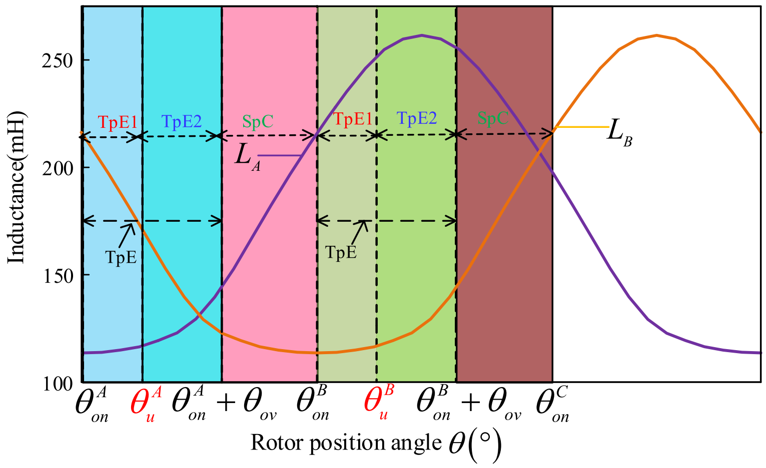

Figure 3. Region allocation based on inductance characteristics.

1) Region 1 ($\theta_{on}^B \sim \theta_u^B$): For phase B, the change rate of inductance is small, and the torque is small, so the TSF of the phase B should be designed as a slowly rising function, and the real-time torque distributed to the phase B is small. For phase A, as the torque generated by phase B is small, phase A needs to stand most of the torque when the motor is operating, so a TSF with slow decline is designed for phase A to ensure that the real-time torque distributed to phase A is large. Through this method, the torque reduced by phase A is controlled to increase in phase B. Thus, the TSF in this region is as follows:

$$\begin{cases} q_{up1}\left(\theta\right) = \left[e^{\frac{k}{-(\theta-\theta_{on})}}+1\right]^{P1} \\ q_{down1}\left(\theta\right) = 1-\left[e^{\frac{k}{-(\theta-\theta_{on})}}+1\right]^{P1} \end{cases} \tag{7}$$

where $q_{up1}(\theta)$ is the function of excitation phase, $q_{down1}(\theta)$ the function of demagnetization phase in region 1, $P1$ the power of formula (7) in region 1, which affects torque reference, and its value is the optimal value obtained from experiments.

2) Region 2 ($\theta_u^B \sim \theta_{on}^B + \theta_{ov}$): At this time, the change rate of inductance increases; the current increases accordingly; and the excitation torque increases rapidly. Since the ability of phase B to provide torque has become greater, it can bear most of the torque. Therefore, the TSF of phase B should be designed as a rapidly rising function, so that phase B can rapidly increase and bear the main torque. For phase A, the TSF of phase A should be designed as a rapidly decreasing function, so that the torque of phase A can decrease rapidly and avoid a large negative torque. Then the TSF in this region is as follows:

$$\begin{cases} q_{up2}\left(\theta\right) = \left[e^{\frac{\theta_{ov}}{-(\theta-\theta_{on})}}+1\right]^{P2} \\ q_{down2}\left(\theta\right) = 1-\left[e^{\frac{\theta_{ov}}{-(\theta-\theta_{on})}}+1\right]^{P2} \end{cases} \tag{8}$$

where $q_{up2}(\theta)$ is the function of excitation phase, $q_{down2}(\theta)$ the function of demagnetization phase in region 2, $P2$ the power of formula (8) in region 2, which affects torque reference, and its value is the optimal value obtained from experiments.

3) SpC ($\theta_{on}^B + \theta_{ov} \sim \theta_{off}^B$): In this region, only phase B is conducting, while phases A and C are disconnected. Then the TSF in this region is as follows:

$$q_2\left(\theta\right) = 1 \tag{9}$$

where $q_2(\theta)$ is the TSF of phase B in SpC.

To sum up, the TSF based on inductance characteristics designed in this paper is expressed as follows:

$$f_k(\theta)\begin{cases} q_1(\theta)=0 & 0\leq\theta\leq\theta_{on}^B \\ q_{up1}(\theta)=\left[e^{\frac{k}{-(\theta-\theta_{on})}+1}\right]^{P1} & \theta_{on}^B\leq\theta\leq\theta_u^B \\ q_{down1}(\theta)=1-\left[e^{\frac{k}{-(\theta-\theta_{on})}+1}\right]^{P1} & \theta_u^B\leq\theta\leq\theta_{on}^B+\theta_{ov} \\ q_{up2}(\theta)=\left[e^{\frac{\theta_{ov}}{-(\theta-\theta_{on})}+1}\right]^{P2} & \theta_u^B\leq\theta\leq\theta_{on}^B+\theta_{ov} \\ q_{down2}(\theta)=1-\left[e^{\frac{\theta_{ov}}{-(\theta-\theta_{on})}+1}\right]^{P2} & \theta_u^B\leq\theta\leq\theta_{on}^B+\theta_{ov} \\ q_2(\theta)\,1 & \theta_{on}^B+\theta_{ov}\leq\theta\leq\theta_{off}^B \\ q_3(\theta)=0 & \theta_{off}^B\leq\theta\leq\tau \end{cases} \tag{10}$$

Figure 4 shows the comparison between conventional TSF and non-unity TSF. As can be seen from the figure, under the control of the new TSF, the torque of the excitation phase is gently rising in region 1, while the torque of the demagnetization phase is gently reduced. In region 2, the torque of the excitation phase is rapidly rising, while the torque of the demagnetization phase is rapidly reduced. After improvement, the total reference torque distribution is more reasonable, thus achieving the goal of minimizing torque ripple.

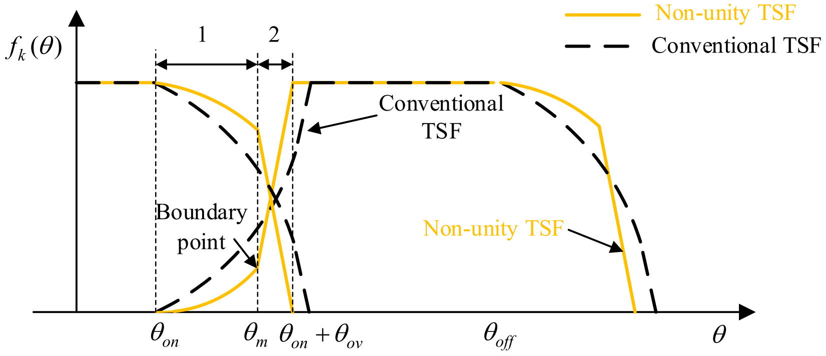

Figure 4. The comparison between conventional TSF and proposed TSF.

4.2. Simulation Results and Analysis

In order to verify the suppression effect of the non-unity TSF method on torque ripple, a three-phase 6/20 SRM is taken as the control object, and the simulation models of conventional exponential TSF and non-unity TSF are established in MATLAB/Simulink. The two control methods are compared and simulated in the same environment. The given load is 3 N·m and 5 N·m, respectively, and the motor is operated at 600 rpm, 900 rpm, and 1200 rpm. The torque ripple and current waveform of the two control methods are compared respectively. In the simulation and experimental analysis, the specific topological structure and parameter table of the three-phase 6/20 SRM used are as follows. Figure 5 shows the topology diagram, and Table 1 is the motor parameter table.

In order to compare the suppression effects of the two control methods on torque ripple and copper loss, the root mean square current (formula (12)) is used to evaluate copper loss; K_r is defined as the torque ripple rate, and its expression is:

$$K_r=\frac{T_{\max}-T_{\min}}{T_{av}}\times 100\% \tag{11}$$

where $T_{\max}$, $T_{\min}$, and T_{av} are the maximum torque, minimum torque, and average torque, respectively.

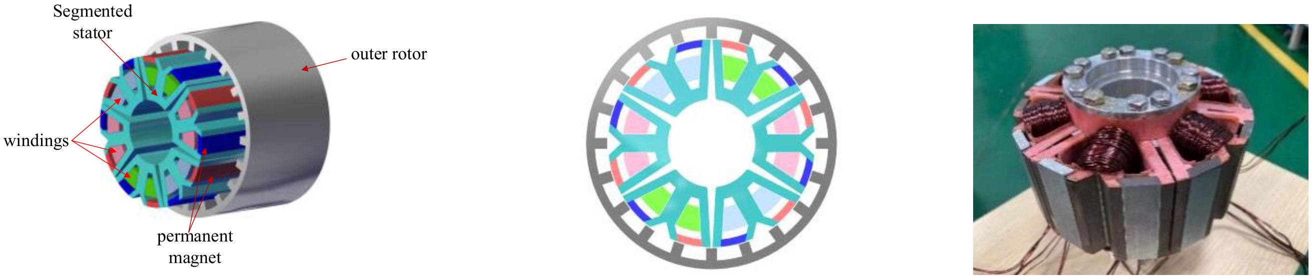

(a) (b) (c)

Figure 5. The 6/20 SRM topology. (a) 3D model. (b) Two-dimensional model. (c) Actual prototype.

Table 1. SRM parameters.

Parameters	Value	Parameters	Value
phase number	3	stator outer diameter (mm)	142
rotor outer diameter (mm)	172	rotor arc angle (°)	6
air gap length (mm)	0.6	stator arc angle (°)	5
number of rotor poles (mm)	20	dc-link voltage (V)	540

Firstly, the simulation waveforms of the motor operating at 3 N·m are compared. As can be seen from Figures 6(a)–(d), when the speed is 600 rpm, the torque ripple of the conventional TSF is 26%, while that of the non-unity TSF method is 23%. These two methods can suppress torque ripple. When the motor speed is 900 rpm, the torque ripple of the conventional TSF method is 58.3%, and that of the non-unity TSF method is 26.3%. When the speed increases, the torque ripple of the conventional TSF method increases, while the torque ripple of the non-unity TSF method changes little, which plays a role in restraining torque ripple. When the motor speed is 1200 rpm, the torque ripple of conventional TSF continues to increase, while the torque ripple of non-unity TSF method is still controlled very little.

Secondly, by comparing the simulation waveforms when the load increases to 5 N·m, it can be seen from Figures 7(a), (d) and (b), (e) that when the motor is operated at 600 rpm and 900 rpm, the torque ripple under the conventional TSF method is obviously increased, while the torque ripple in the non-unity TSF method can still be kept small. Under the condition of high speed and increasing load, the torque ripple of non-unity TSF increases, but compared with the conventional TSF, the non-unity TSF still suppresses the torque ripple in a small range.

As can be seen from the torque waveforms in Figures 6 and 7, compared with the conventional TSF method, the non-unity TSF method can restrain the torque ripple more effectively. However, comparing the current waveforms of the two methods, the non-unit TSF method also has the problems of large peak current and high copper loss, which reduces the operating efficiency of the motor.

5. OPTIMIZATION OF OVERLAPPING ANGLE IN TPE

According to the inductance characteristics in different regions, a non-unity TSF with three regions is designed, which ensures the rationality of the TSF of the excitation phase and the demagnetization phase and suppresses the torque ripple in the TpE. Although the torque ripple is effectively suppressed by the non-unity TSF with three regions, the peak current is not considered, so the copper loss is large, and the copper loss directly affects the operation efficiency of the motor. Therefore, based on the non-unity TSF, an overlapping angle optimization algorithm is proposed to reduce the peak current and copper loss.

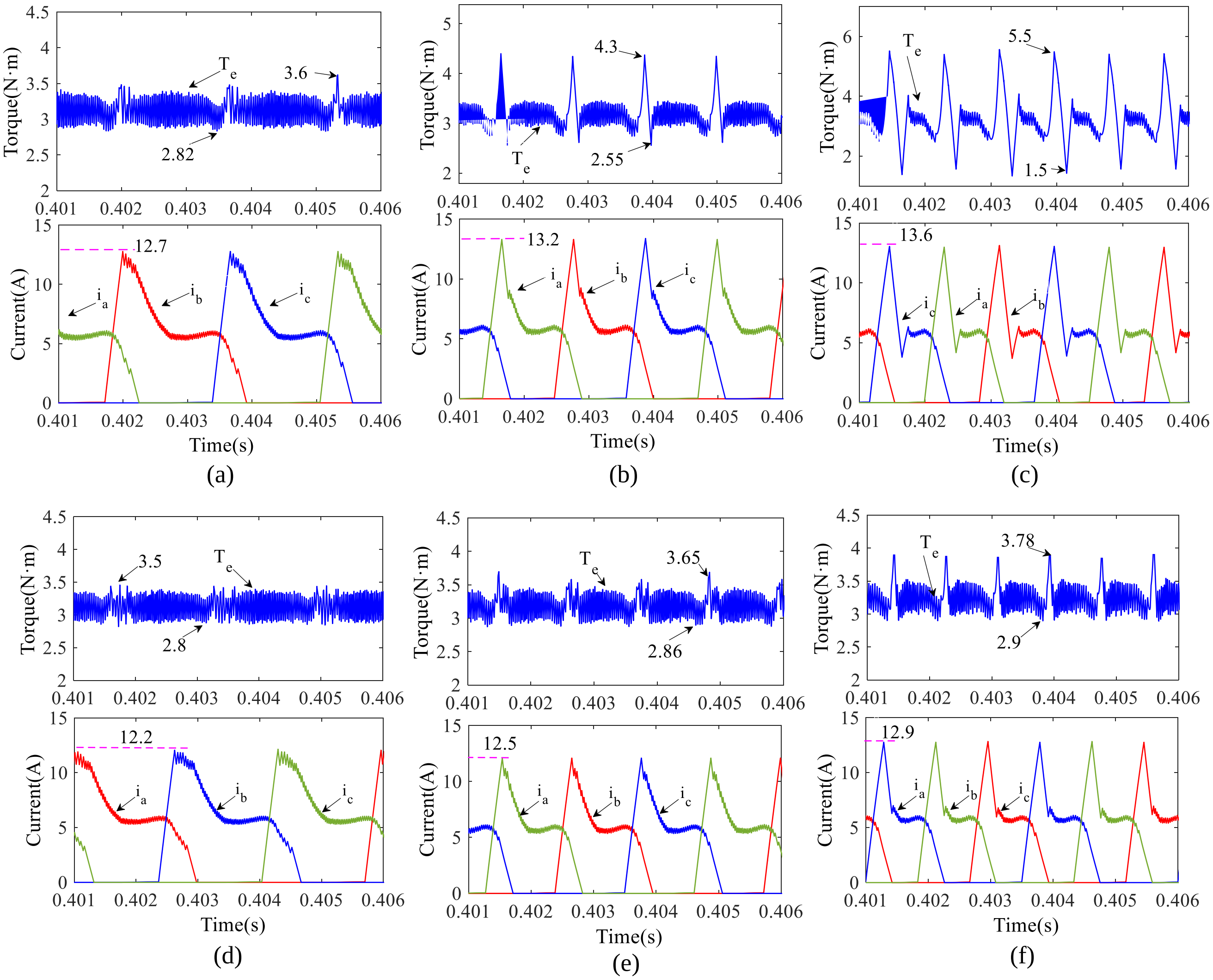

(a) (b) (c) (d) (e) (f)

Figure 6. The current waveform and torque waveform at different speeds when the load is 3 N·m. (a) Conventional TSF, 600 rpm. (b) Conventional TSF, 900 rpm. (c) Conventional TSF, 1200 rpm. (d) Non-unity TSF, 600 rpm. (e) Non-unity TSF, 900 rpm. (f) Non-unity TSF, 1200 rpm.

5.1. Optimization Algorithm of Overlapping Angle

The overlapping angle is the main parameter in TSF, and the reasonable setting of the overlapping angle has an important influence on reducing the magnitude of the peak current and copper loss. If the overlapping angle is too large, the demagnetized phase current will still have a large current in the inductance falling region, resulting in a large negative torque. If the overlap angle is too small, the rising time of the excitation phase current will be shortened, and the excitation phase torque will be insufficient. In order to track the torque reference, the excitation phase current will rise to a larger value, resulting in the generation of peak current and aggravating the copper loss. In addition, with the increase of speed, the above two situations will be aggravated, which will further increase the copper loss.

The performance index of copper loss in SRM can be evaluated by root mean square current, and the expression is:

$$I_{rms} = \sqrt{\frac{1}{\theta_{ov}} \int_{\theta_{on}}^{\theta_{on}+\theta_{ov}} \left(i_k^2\left(T,\theta\right) + i_{k-1}^2\left(T,\theta\right)\right) d\theta} \tag{12}$$

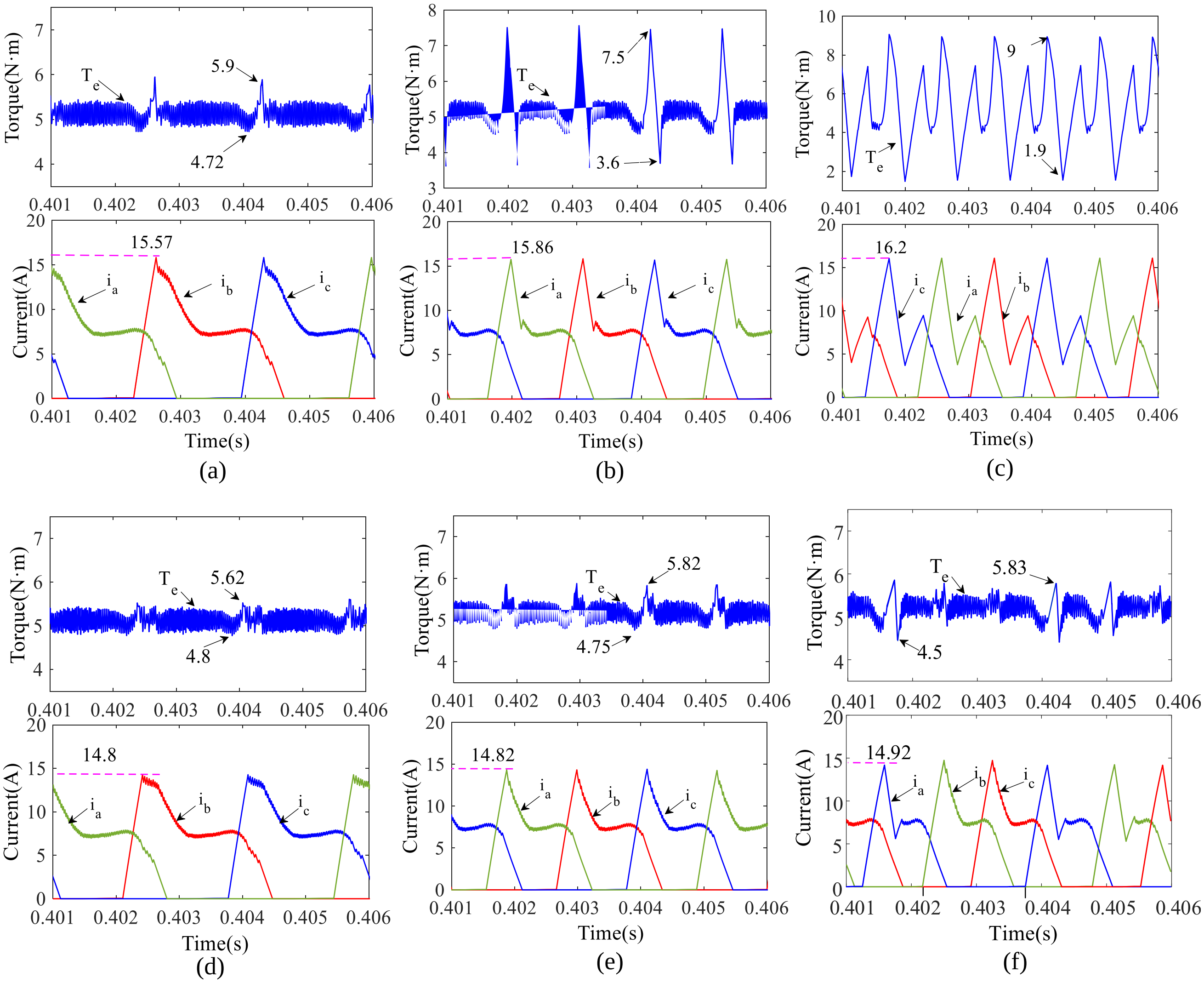

(a)

(b)

(c)

(d)

(e)

(f)

Figure 7. The current waveform and torque waveform at different speeds when the load is 5 N·m. (a) Conventional TSF, 600 rpm. (b) Conventional TSF, 900 rpm. (c) Conventional TSF, 1200 rpm. (d) Non-unity TSF, 600 rpm. (e) Non-unity TSF, 900 rpm. (f) Non-unity TSF, 1200 rpm.

where i_k is the excitation phase current, and i_{k-1} is the demagnetization phase current.

According to formula (11), the integral value of the sum of squares of the current can be reduced by adjusting the overlapping angle θ_{ov}, thereby reducing copper loss. The smaller the overlap angle θ_{ov} is, the smaller the value of formula (11) is, but the winding is an inductive device, which has a certain charging and discharging time, and θ_{ov} is impossible to be reduced to zero during the operation of the motor, so it is necessary to determine the appropriate overlapping angle θ_{ov} to make copper loss reduced.

Taking excitation phase A as an example, the torque of excitation phase A is zero at the turn-on angle θ_{on}, and then it enters the two-phase exchange region, that is, the overlapping angle region in TSF. When the torque control in the overlapping angle region is completed, the torque value of excitation A is T_{ref}, and the rotor position angle at this time is the end point of the overlapping angle $\theta_{on} + \theta_{ov}$. The size of overlapping angle θ_{ov} can be obtained by calculating the size of $\theta_{on} + \theta_{ov}$, so it is necessary to get the size of rotor position angle when the excitation phase torque of two-phase exchange region is T_{ref}. The specific algorithm steps are as follows:

1) Set angular velocity ω, torque reference T_{ref}, sampling time Δt.

2) Calculate the new flux linkage value φ_{k+1} and rotor position value θ_{k+1}.
   The increment of flux $\Delta\varphi$ can be obtained by Formula (1), and the new flux value φ_{k+1} can be obtained by adding the old flux value φ_k and the incremental value $\Delta\varphi$ of step flux, that is:
$$\begin{cases} \Delta\varphi = (U - iR)\,\Delta t \\ \varphi_{k+1} = \varphi_k + \Delta\varphi \end{cases} \tag{13}$$
   The rotor position increment $\Delta\theta$ can be obtained according to the angular velocity ω, and the new rotor position θ_{k+1} can be obtained by adding the old rotor position θ_k and the rotor position increment $\Delta\theta$:
$$\begin{cases} \Delta\theta = \omega\Delta t \\ \theta_{k+1} = \theta_k + \Delta\theta \end{cases} \tag{14}$$
3) In order to get the latest current value, a current look-up table (LUT) algorithm is carried out according to the flux value φ_{k+1} and rotor position angle θ_{k+1} obtained in the previous step, and a new current value i_{k+1} is obtained:
$$i_{k+1} = i\left(\varphi_{k+1}, \theta_{k+1}\right) \tag{15}$$
4) According to the current value i_{k+1} and rotor position angle θ_{k+1} obtained in the previous step, the torque value is obtained through the torque LUT algorithm:
$$T_{k+1} = T\left(i_{k+1}, \theta_{k+1}\right) \tag{16}$$
5) Judge whether T_{k+1} is greater than T_{ref}. If it is, output the rotor position angle θ_{k+1} at this time and proceed to step 6; otherwise, return to step 2 for a loop.
6) The magnitude of the overlapping angle θ_{ov} is obtained by formula (16):
$$\begin{cases} \theta_{k+1} = \theta_{on} + \theta_{ov} \\ \theta_{ov} = \theta_{k+1} - \theta_{on} \end{cases} \tag{17}$$

According to the above calculation process, the overlapping angle can be obtained, and the data of look-up table used are all nonlinear, which is more suitable for the actual situation and has better control effect than linear or quasi-linear data.

As shown in Figure 8, the flowchart of the overlapping angle adaptive algorithm is proposed in this paper.

According to the above improvements, the overall control block diagram is shown in Figure 9. According to the difference of inductance change rate, the two-phase exchange region is redivided, and a new region allocation is realized. According to the non-unity TSF of formula (10), the torque reference is distributed more reasonably, and the torque ripple is reduced. At the same time, according to the proposed overlapping angle adaptive algorithm, the appropriate overlapping angle under different speeds and different loads is obtained, which further reduces copper loss.

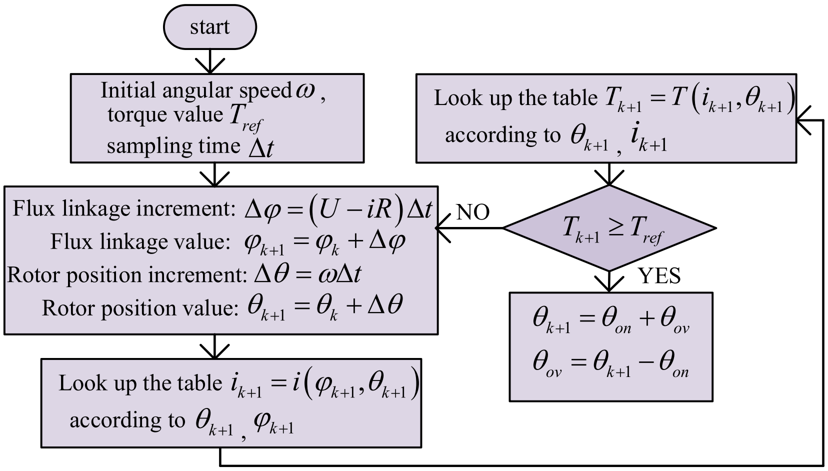

Figure 8. Flow chart of the overlapping angle adaptive algorithm.

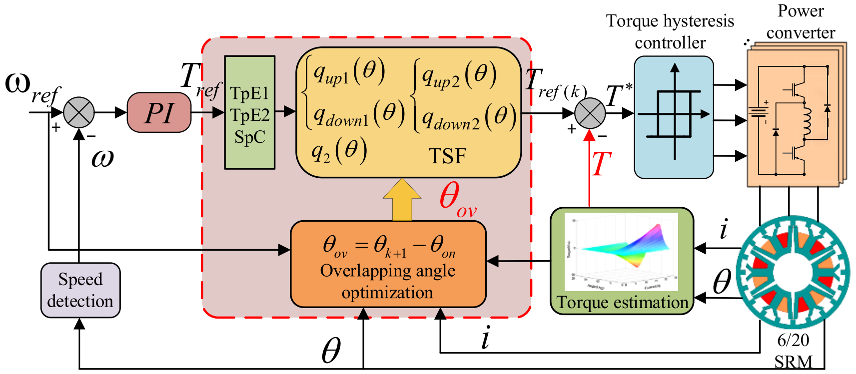

Figure 9. The control block diagram of non-unity TSF control method with adaptive overlapping angle.

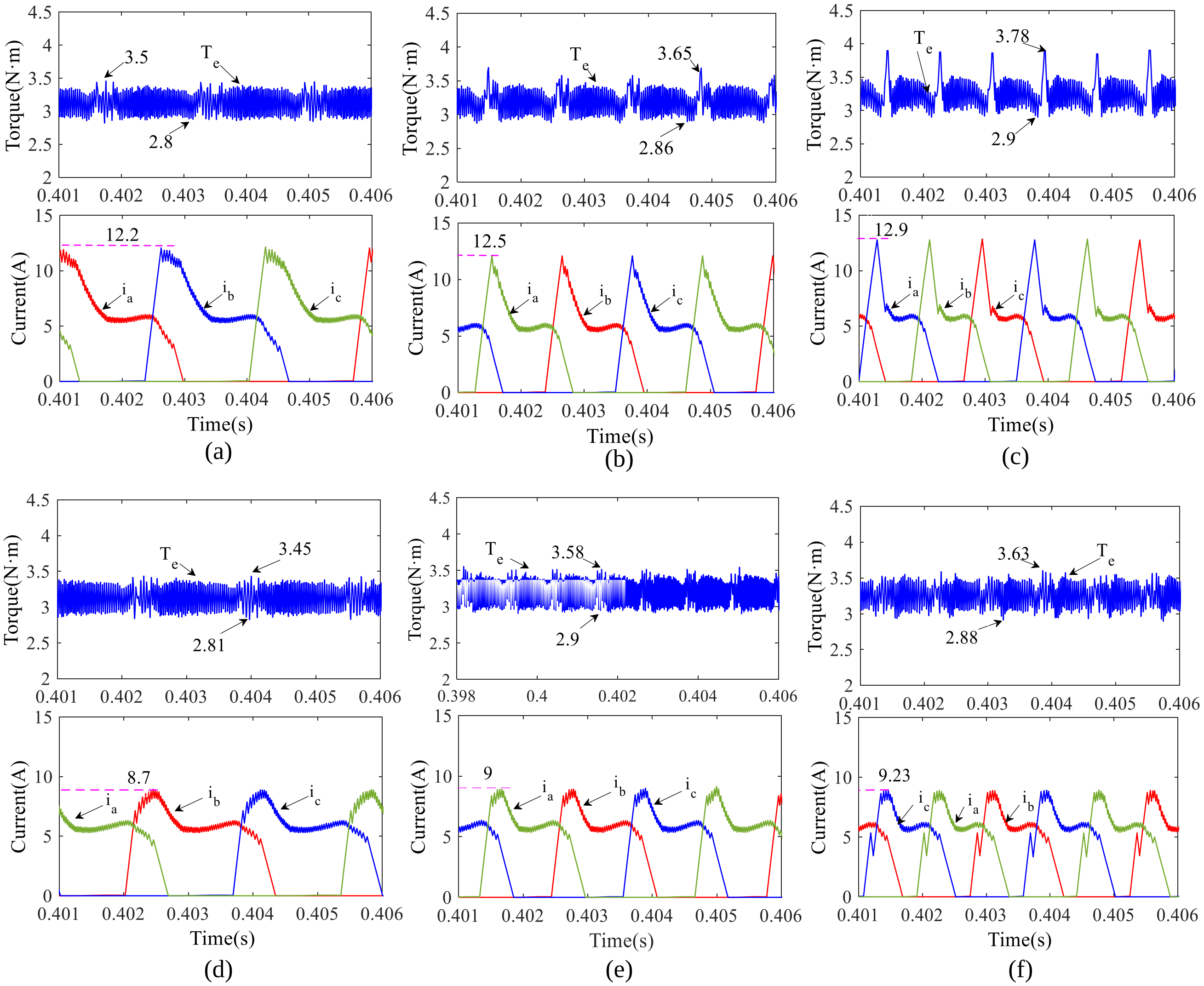

Figure 10. The current waveform and torque waveform at different speeds when the load is 3 N·m. (a) Non-unity TSF, 600 rpm. (b) Non-unity TSF, 900 rpm. (c) Non-unity TSF, 1200 rpm. (d) Non-unity TSF-AOA, 600 rpm. (e) Non-unity TSF-AOA, 900 rpm. (f) Non-unity TSF-AOA, 1200 rpm.

5.2. Simulation Results and Analysis

In order to verify the effectiveness of the proposed non-unity TSF with adaptive overlapping angle (non-unity TSF-AOA) method, the non-unity TSF method and non-unity TSF-AOA method are compared and simulated in Simulink. The given load is 3 N·m and 5 N·m, respectively, and the motor is operated at 600 rpm, 900 rpm and 1200 rpm.

The simulation waveform of the motor operating at 3 N·m is shown in Figure 10. Firstly, when the speed is 600 rpm, the torque and current waveform of the two control modes are shown in Figures 10(a)–(d). By comparison, the non-unity TSF method has a larger peak current (12.2 A) in the two-phase exchange region. However, the non-unity TSF-AOA method keeps a small peak current (8.7 A), and the peak current is reduced by 3.5 A.

Secondly, when the speed is 900 rpm, the torque and current waveform diagram of the two control modes are shown in Figures 10(b)–(e). By comparison, when the speed increases, the peak current of non-unity TSF is 12.5 A in the exchange region, and the torque ripple and peak current increase. While the peak current of non-unity TSF-AOA is 9 A, and the torque ripple and peak current are still controlled within a small range.

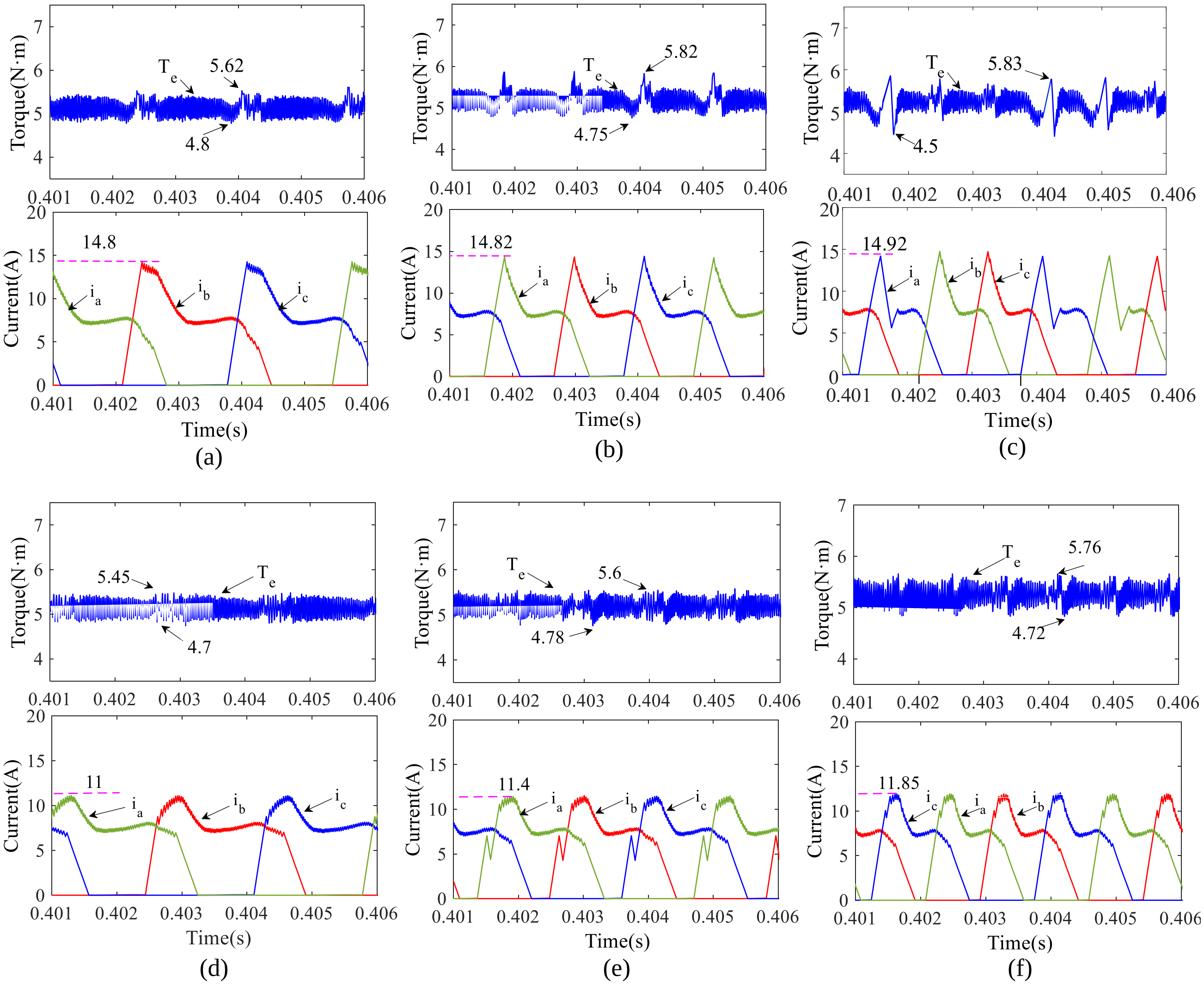

Figure 11. The current waveform and torque waveform at different speeds when the load is 5 N·m. (a) Non-unity TSF, 600 rpm. (b) Non-unity TSF, 900 rpm. (c) Non-unity TSF, 1200 rpm. (d) Non-unity TSF-AOA, 600 rpm. (e) Non-unity TSF-AOA, 900 rpm. (f) Non-unity TSF-AOA, 1200 rpm.

Thirdly, when the speed is 1200 rpm, the torque and current waveform diagram of the two control methods are shown in Figures 10(c)–(f). By comparison, although the torque ripple of the non-unity TSF control method is at a small value, its peak current continues to increase at high speed. The torque ripple and peak current of the proposed non-unity TSF-AOA control method have increased, and they are still controlled in a small range. Therefore, the proposed non-unity TSF-AOA can suppress torque ripple and peak current at high speed.

Finally, the effects of different loads on the torque and current waveform of SRM under two control modes are compared. As can be seen from Figure 11, the peak current value of the non-unity TSF control method obviously increases under the working conditions of medium and low speed and load increase, while the non-unity TSF-AOA can still control the peak current at a small value when the load increases. At high speed, when the load increases, the peak current increases to 11.85 A, which is 3.07 A lower than that of the non-unity TSF 14.92 A. At the same time, the two control methods have a good effect on restraining the torque ripple. Therefore, the proposed non-unity TSF with overlapping angle adaptive control method still has good torque ripple and peak current suppression effect under high speed and large load.

The performance comparison between the proposed control method and the conventional TSF control method is shown in Table 2.

Table 2. Performance comparison between the proposed control method and conventional TSF.

Method	Speed	Load	$k(\%)$	I_{rms} (A)
Proposed method	600 rpm	3 N·m	21.3	5.92
Conventional TSF	600 rpm	3 N·m	26	9.35
Proposed method	600 rpm	5 N·m	15	8.3
Conventional TSF	600 rpm	5 N·m	23.6	13.4
Proposed method	900 rpm	3 N·m	22.6	6.21
Conventional TSF	900 rpm	3 N·m	58.3	9.6
Proposed method	900 rpm	5 N·m	16.4	8.63
Conventional TSF	900 rpm	5 N·m	130	14.1
Proposed method	1200 rpm	3 N·m	25	6.47
Conventional TSF	1200 rpm	3 N·m	130	9.86
Proposed method	1200 rpm	5 N·m	20.8	8.87
Conventional TSF	1200 rpm	5 N·m	142	14.5

It can be seen from the table that when the load is 3 N·m, compared with the conventional TSF control method, the torque ripple of the proposed control method can be reduced by up to 105%, and I_{rms} can be reduced by up to 3.39 A. When the load increases, compared with the conventional TSF control method, the torque ripple of the proposed control method can be reduced by up to 121.2%, and I_{rms} can be reduced by 5.63 A. The effectiveness of the proposed method is verified.

In order to verify the ability of the proposed control method to suppress torque ripple and copper loss, a performance comparison table between the proposed control method and other improved TSF control methods is established, as shown in Table 3, and the relevant comparison parameters are as follows:

1) The copper loss of SRM is evaluated by the root mean square current I_{rms}, that is Formula (11). J_p is defined as the reduction ratio of copper loss between the improved method and the conventional method, and J_p expression is as follows:

$$J_p = \frac{I_b - I_a}{I_b} \tag{18}$$

where I_b and I_a are the copper losses of the conventional method and the improved method, respectively.

2) At the same time, J_k is defined as the reduction ratio of torque ripple rate between the improved method and the conventional method, and the expression is:

$$J_k = \frac{k_b - k_a}{k_b} \tag{19}$$

where k_b and k_a are the torque ripple rates of the conventional method and the improved method, respectively.

According to Table 3, compared with the other improved TSFs, the reduction ratio of torque ripple and copper loss of proposed TSF is greater than that of the other three improved TSFs. Therefore, the control method proposed in this paper can not only reduce the torque ripple, but also reduce the copper loss and improve efficiency.

Table 3. Performance comparison of the proposed control method with other improved TSF.

Method	$J_{k\_\max}$	$J_{p\_\max}$
Proposed TSF	85%	38.8%
OCTSF [20]	66.67%	6.19%
TSF-MPC [19]	54%	7.14%
Modified TSF [21]	67.21%	7.49%

6. EXPERIMENTAL VERIFICATION

Figure 12 shows the SRM experimental platform in this paper. The whole experimental platform includes SRM prototype, TMS320F28335 control board, power converter, torque sensor, tension controller, magnetic powder brake, current sensor, absolute encoder, etc.

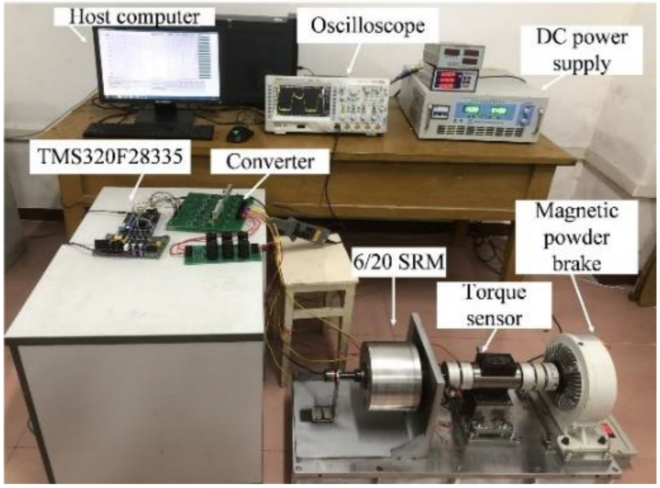

Figure 12. Experimental platform.

In order to verify the correctness of the control method proposed in this paper, the load is set to 3 N·m, and the speed is set to 600 rpm. Experiments are carried out under the conventional TSF and proposed methods, respectively, and the experimental results are shown in Figures 13–14.

It can be seen from Figure 13 that under the conventional TSF method, the torque ripple is 30%, and the peak current is 13.2 A. Under the proposed method, the torque ripple is 25%, and the peak

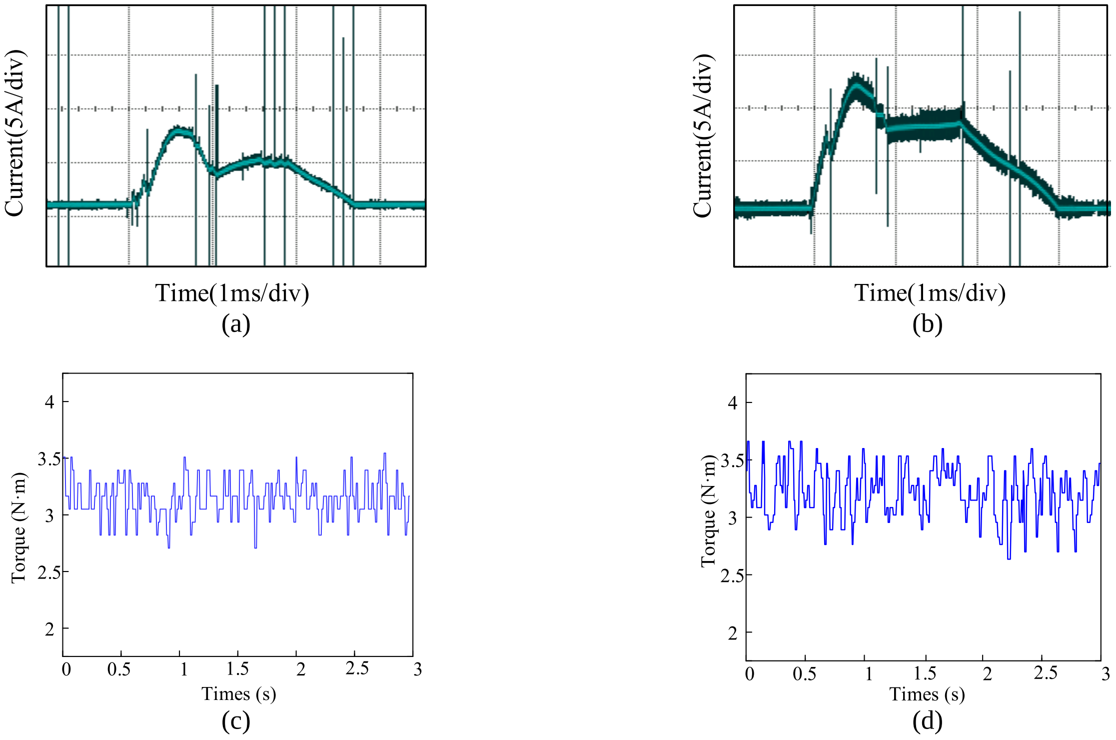

(a) (b) (c) (d)

Figure 13. Current and torque waveforms of proposed non-unity TSF with overlapping angle adaptive at 600 rpm when the load is 3 N·m. (a) Current waveforms of proposed TSF. (b) Current waveforms of conventional TSF. (c) Torque waveforms of proposed TSF. (d) Torque waveforms of conventional TSF.

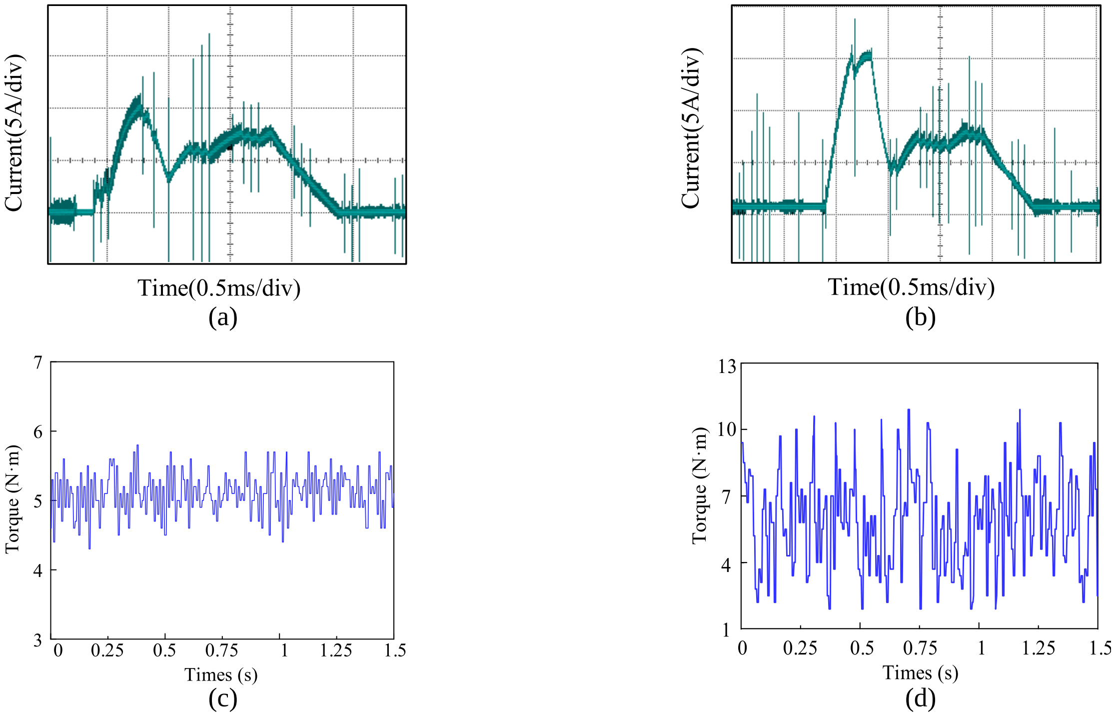

(a) (b) (c) (d)

Figure 14. Current and torque waveforms of proposed non-unity TSF with overlapping angle adaptive at 1200 rpm when the load is 5 N·m. (a) Current waveforms of proposed TSF. (b) Current waveforms of conventional TSF. (c) Torque waveforms of proposed TSF. (d) Torque waveforms of conventional TSF.

current is 9 A. By comparing the two control methods, the torque ripple and peak current of the proposed control method are reduced.

In order to verify the performance of proposed method under the condition of high speed and large load. The two methods are carried out under the conditions of 1200 rpm, and load torque is 5 N·m. The experimental results are shown in Figure 14. When the speed and load increases, the peak current of the conventional TSF method is 16 A, and the torque ripple is 150% which obviously increases. The torque ripple of the proposed method is 26%, and the peak current is 11 A. In comparison, when the speed and load increase, the control method proposed in this paper reduces the torque ripple by 124% and the peak current by 5 A. Therefore, the proposed control method in this paper can still suppress the torque ripple and reduce the copper loss when the speed and load torque increase.

7. CONCLUSION

Aiming at the problems of torque ripple, peak current, and high copper loss in conventional TSF, this paper proposes a non-unity TSF control method with overlapping angle adaptive. By analyzing the characteristics of inductance and torque, this method divides the conduction region into three regions and designs the corresponding function in each region. At the same time, the overlapping angle adaptive algorithm can get the appropriate overlap angle according to different speeds and loads. Taking a new three-phase 6/20-pole SRM as the research object, the proposed method is simulated and verified by experiments, and the following conclusions can be drawn:

1) The non-unity TSF based on overlapping angle adaptation can reduce the torque ripple at different speeds. It can reduce 85% under low load (3 N·m) and reduce 87% under large load (5 N·m).
2) The proposed control method can reduce the peak current and root mean square current at different speeds, and the peak current can be reduced by 4.37 A at low load and 4.57 A at large load. The root mean square current can be reduced under low load and heavy load of 3.43 A and 5.63 A, respectively. Therefore, the proposed control method can effectively reduce copper loss.
3) Compared with conventional TSF method, the control method proposed in this paper can reduce copper loss and improve motor efficiency while suppressing torque ripple and peak current.

ACKNOWLEDGMENT

This work was supported by the National Natural Science Foundation of China under Project 52167005.

REFERENCES

1. Boldea, I., L. N. Tutelea, L. Parsa, and D. Dorrell, "Automotive electric propulsion systems with reduced or no permanent magnets: An overview," *IEEE Transactions on Industrial Electronics*, Vol. 61, No. 10, 5696–5711, 2014.
2. Omac, Z., M. Polat, E. Oksuztepe, M. Yildirim, O. Yakut, H. Eren, M. Kaya, and H. Kurum, "Design, analysis, and control of in-wheel switched reluctance motor for electric vehicles," *Electrical Engineering*, Vol. 100, No. 2, 865–876, 2018.
3. Santiago, J. D., H. Bernhoff, B. Ekergård, S. Eriksson, S. Ferhatovic, R. Waters, and M. Leijon, "Electrical motor drivelines in commercial all-electric vehicles: A review," *IEEE Transactions on Vehicular Technology*, Vol. 61, No. 2, 475–484, 2012.
4. De Paula, M. V., T. A. Barros, H. S. Moreira, et al., "A dahlin cruise control design method for switched reluctance motors with minimum torque ripple point tracking applied in electric vehicles," *IEEE Transactions on Transportation Electrification*, Vol. 7, No. 2, 730–740, 2021.
5. Vaibhav, S. and P. Saifullah, "An integrated driving/charging four-phase switched reluctance motor drive with reduced current sensors for electric vehicle application," *IEEE Journal of Emerging and Selected Topics In Power Electronics*, Vol. 10, No. 6, 6880–6890, 2022.

6. Cheok, A. D. and Y. Fukuda, "A new torque and flux control method for switched reluctance motor drives," *IEEE Transactions on Power Electronics*, Vol. 17, No. 4, 543–557, 2002.
7. Yan, N., X. Cao, and Z. Deng, "Direct torque control for switched reluctance motor to obtain high torque-ampere ratio," *IEEE Transactions on Industrial Electronics*, Vol. 66, No. 7, 5144–5152, 2019.
8. Chen, X., Z. Zhang, L. Yu, and Z. Bian, "An improved direct instantaneous torque control of doubly salient electromagnetic machine for torque ripple reduction," *IEEE Transactions on Industrial Electronics*, Vol. 68, No. 8, 6481–6492, 2021.
9. Tao, T., S. Gan, J. Wang, X. Song, J. Zhang, and Z. Sun, "Angle position control of fuzzy algorithm with variable scale factor for SRM," *ICIC Express Letters*, No. 4, 789–797, 2017.
10. Yang, D. H. Y., D. Zhao, and Y. X. Jiang, "A research for angle optimization of the SRM used in electric actuator of valves," *Applied Mechanics and Materials*, 586–591, 2013.
11. Blaabjerg, F., P. C. Kjaer, P. O. Rasmussen, and C. Cossar, "Improved digital current control methods in switched reluctance motor drives," *IEEE Transactions on Power Electronics*, Vol. 14, No. 3, 563–572, 1999.
12. Cai, J.-L. and R.-J. Jin, "Reversible drive system of switched reluctance motor based on DSP controller," *Zhejiang Daxue Xuebao (Gongxue Ban)/Journal of Zhejiang University (Engineering Science)*, No. 6, 1019–1026, 2006.
13. Mohamed, Y. A. R. I. and E. F. El-Saadany Robust, "High bandwidth discrete-time predictive current control with predictive internal model — A unified approach for voltage-source PWM converters," *IEEE Transactions on Power Electronics*, Vol. 23, No. 1, 126–136, 2008.
14. Peng, F., J. Ye, and A. Emadi, "A digital PWM current controller for switched reluctance motor drives," *IEEE Transactions on Power Electronics*, Vol. 31, No. 10, 7087–7098, 2016.
15. Schulz, S. E. and K. M. Rahman, "High-performance digital PI current regulator for EV switched reluctance motor drives," *IEEE Transactions on Industry Applications*, Vol. 39, No. 4, 1118–1126, 2003.
16. Xue, X. D., K. W. E. Cheng, and S. L. Ho, "Optimization and evaluation of torque-sharing functions for torque ripple minimization in switched reluctance motor drives," *IEEE Transactions on Power Electronics*, Vol. 24, No. 9, 2076–2090, 2009.
17. Ling, X., C. Zhou, L. Yang, and J. Zhang, "Torque ripple suppression method of switched reluctance motor based on an improved torque distribution function," *Applied Sciences*, Vol. 11, No. 10, 136–152, 2022.
18. Li, H., B. Bilgin, and A. Emadi, "An improved torque sharing function for torque ripple reduction in switched reluctance machines," *IEEE Transactions on Power Electronics*, Vol. 34, No. 2, 1635–1644, 2019.
19. Yang, Y., A. Xu, B. Leng, J. Sun, and K. Li, "Torque compensation method of switched reluctance motor adopting MPC based on TSF-DITC," *Progress In Electromagnetics Research M*, Vol. 110, 211–221, 2022.
20. Sun, Q., J. Wu, C. Gan, Y. Hu, and J. Si, "OCTSF for torque ripple minimisation in SRMs," *IET Power Electronics*, No. 14, 2741–2750, 2016.
21. Fei, C., J. Yan, P. Wang, and Z. Yan, "Torque ripple suppression of switched reluctance motor based on modified torque sharing function," *Diangong Jishu Xuebao/Transactions of China Electrotechnical Society*, Vol. 33, 394–400, 2018.
22. Ro, H. S., K. G. Lee, J. S. Lee, H. G. Jeong, and K. B. Lee, "Torque ripple minimization scheme using torque sharing function based fuzzy logic control for a switched reluctance motor," *Journal of Electrical Engineering & Technology*, Vol. 10, No. 1, 118–127, 2015.